photonics

Communication

Key Space Enhancement in Chaotic Secure Communication Utilizing Monolithically Integrated Multi-Section Semiconductor Lasers

Feifan Zhang [1,2], Yuncai Wang [1,2,*], Yuehui Sun [1,2], Junpei Xu [1,2], Pu Li [1,2], Anbang Wang [1,2] and Yuwen Qin [1,2]

[1] Guangdong Provincial Key Laboratory of Photonics Information Technology, Guangdong University of Technology, Guangzhou 510006, China
[2] School of Information Engineering, Guangdong University of Technology, Guangzhou 510006, China
* Correspondence: wangyc@gdut.edu.cn

Abstract: Chaotic secure communication schemes encounter a conflict of key space enhancement between the consistency and complexity of chaotic transceivers. In this paper, we propose a monolithically integrated multi-section semiconductor laser (MIMSL), used as a compact chaotic transceiver with an enhanced key space. The MIMSL consists of a distributed feedback (DFB) laser section, a semiconductor optical amplifier (SOA) section, two phase (P) sections and a passive optical waveguide. We simulate the dynamics of the MIMSL by applying the time-dependent coupled-wave equations for traveling-wave optical fields. Further, we numerically demonstrate a security enhancement of the unidirectional chaotic communication scheme using the MIMSL transceivers with independent high-speed modulation in the phase sections of the MIMSL. The security of our scheme depends not only on the difficulty of identifying the MIMSL structural parameters and the bias current of each section, but also on the phase shifts in two phase sections providing the additional dimension of security key space. Final simulation results show that a total of 2^{48} key spaces can be achieved with a data rate of 2.5 Gb/s and an injection strength of 0.36.

Keywords: monolithically integrated multi-section semiconductor laser; key space; chaotic secure communication; optical feedback

check for updates

Citation: Zhang, F.; Wang, Y.; Sun, Y.; Xu, J.; Li, P.; Wang, A.; Qin, Y. Key Space Enhancement in Chaotic Secure Communication Utilizing Monolithically Integrated Multi-Section Semiconductor Lasers. *Photonics* **2023**, *10*, 213. https://doi.org/10.3390/photonics10020213

Received: 17 December 2022
Revised: 7 February 2023
Accepted: 10 February 2023
Published: 15 February 2023

Copyright: © 2023 by the authors. Licensee MDPI, Basel, Switzerland. This article is an open access article distributed under the terms and conditions of the Creative Commons Attribution (CC BY) license (https://creativecommons.org/licenses/by/4.0/).

1. Introduction

Chaotic systems are considered good candidates for information security because of their broadband, large random amplitude, unpredictability and sensitivity to initial values [1,2]. Chaotic semiconductor lasers have been widely used in secure communication [3], random number generation [4–7], chaotic lidar [8], distributed fiber sensing [9], fiber network fault detection [10], and ultra-wide band technology [11].

In particular, secure communication based on a chaotic carrier has attracted much attention in recent years because of its high security of hardware encryption at the physical layer. Its security mainly depends on the parameter adaptation range of the transceivers and the sensitivity of synchronization quality to parameter mismatch [12,13]. However, the key space enhancement of the chaotic secure communication scheme remains a challenge now that the structural complexity of the chaotic laser as a transceiver decreases the synchronization quality.

Common chaotic lasers are composed of discrete components, which lead to bulk and a lack of long-term stability. This makes it difficult to achieve a relatively high synchronization coefficient for the transceivers [14]. Generally, the semiconductor laser is attached to an optical fiber of several meters, which corresponds to a time-delayed feedback of tens of nanoseconds. This long feedback cavity causes instability in the feedback phase due to temperature fluctuations and small external interferences [15]. As a result, its key space is limited, because the laser bias current and the feedback delay time are unsuitable as key parameters due to the exposure risk [16–18]. To enhance the key space, Wang et al. proposed a semiconductor laser by dispersive feedback from a chirped FBG to conceal the time-delay signature of the chaotic system [19]. Yi et al., proposed to maximize the security of chaotic optical communication by multiple G-T etalons [20]. Wang et al. reported another chaotic system with two delayed interfering branches to enhance the security by electro-optical feedback phase modulation [21]. However, all of these schemes are very complex and their operation is unstable and very sensitive to environmental variations in practice.

Integrated chaotic lasers may be promising solutions to the aforementioned issue, because they possess many unique merits such as compact size, low cost, and stable operation. For instance, a built-on-chip chaotic laser source-integrated semiconductor laser with optical feedback system was presented in Ref. [22]. This chaotic laser exhibited diverse dynamics in the 1 cm short-cavity condition and has been deployed for secure communication [23]. In Ref. [24], Tronciu et al., reported another integrated semiconductor laser with an air gap subject to multiple optical feedback loops that could display chaotic behaviors appropriate for chaos-based communication. In Refs. [25–27], a chaos laser chip with a straight waveguide was presented for physical random bit generation. Furthermore, integrated amplified feedback lasers were also reported for the microwave and broadband chaos generation with a short active cavity [28–30]. However, there has been little research on using integrated chaotic lasers for key space enhancement in secure communication.

In this paper, we propose a monolithically integrated multi-section semiconductor laser (MIMSL) to enhance the security of chaotic communication. The MIMSL is composed of a DFB laser section, SOA section, two phase sections, and a passive optical waveguide. The detailed nonlinear dynamical behaviors of the MIMSL are numerically investigated using time-dependent coupled-wave equations. We demonstrate that chaos synchronization can be realized using this kind of MIMSL for unidirectional communication. Furthermore, we conduct a study to evaluate the impact of the mismatch of MIMSL parameters on synchronization performance. In particular, we use the independent private key in the phase sections of the MIMSL as a private key to enhance the physical key space. Our simulation results confirms that the key space can reach 2^{48} in a unidirectional chaotic secure communication with a data rate of 2.5 Gb/s.

2. Methods

2.1. Principle

The structure of MIMSL is shown in Figure 1a, comprising a DFB laser section, a SOA section, two independent phase sections (P1 and P2), and a passive waveguide (WG). The DFB laser section is designed as a laser source, operating at a single longitudinal mode. The WG acts as an external cavity, which provides optical feedback and triggers laser chaos. The P1, P2 and SOA section are used to control the phase and intensity of the optical feedback, respectively. Quantitatively, the lengths of the DFB, P1, SOA, P2 and passive WG are 200, 150, 350, 300 μm and 4 mm, respectively. The left facet of this chip is anti-reflection (AR)-coated to maximize the output power, while its right facet is cleaved with a reflectivity ratio of 0.32. The length of the external cavity delimited by the internal facet of the DFB section and the chip cleaved facet is 4.8 mm, corresponding to a round-trip delay time of 0.118 ns (i.e., an external cavity frequency of 8.47 GHz). The refractive index of WG is 3.7, which is approximately the same as that of the other sections. In addition, all the facet reflections between the different sections are negligible.

Figure 1b shows the schematic of the proposed secure chaotic communication system. At the transmitter terminal, a MIMSL termed as master semiconductor laser (MSL) is adopted to provide the original chaotic carrier, and a Mach–Zehnder modulator is used to encrypt the message onto the original chaotic carrier. Different from conventional chaotic communication systems based on external cavity semiconductor lasers, the MSL contains two phase modulators that are driven by different secret keys in the P1 and P2 sections, respectively. With the phase modulation, the spectrum of the modulated chaotic carrier is greatly expanded in the optical domain. Then, the modulated chaotic carrier (chaos + message) is sent to the receiver. At the receiver terminal, the transmitted chaotic carrier is injected into a receiver MIMSL referred to as slave semiconductor laser (SSL) to achieve chaos synchronization. The amplitude of the chaotic carrier at SSL is inverted by the IPD and summed with the signal at the MSL to eliminate the chaotic carrier signal for message decryption [23]. Meanwhile, to ensure the consistency of the transceiver parameters, the SSL is driven by phase modulators with the same secret keys as the MSL of the P1 and P2 sections.

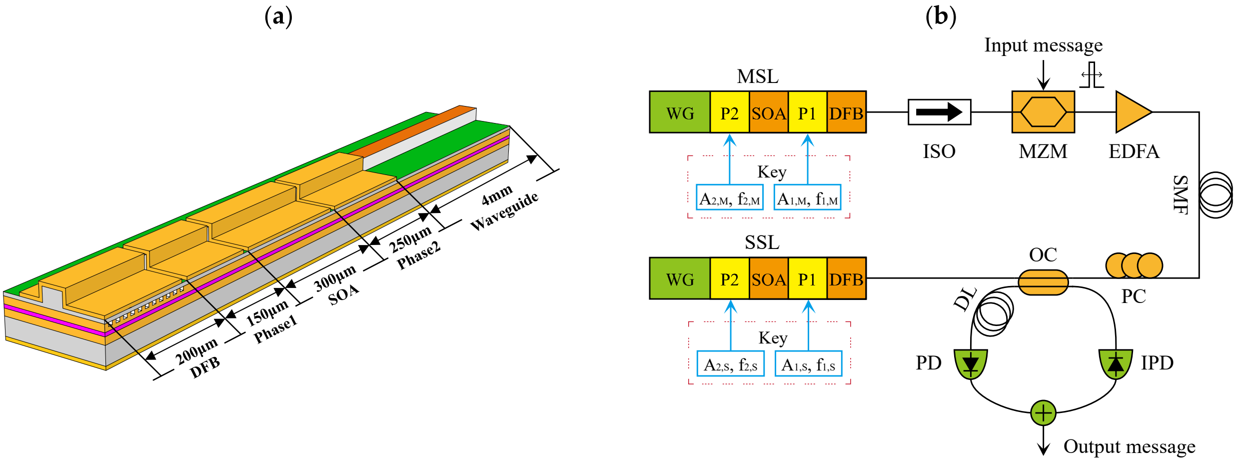

Figure 1. (**a**) The structure of the MIMSL and (**b**) schematic of the chaotic secure communication system. MSL (SSL), master (slave) semiconductor laser; ISO, isolator; MZM, Mach–Zehnder modulator; EDFA, erbium-doped fiber amplifier; SMF, single-mode fiber; PC, polarization controller; OC, optical coupler; DL, optical delay line; PD, photodiode; IPD, inverted photodiode.

2.2. Theoretical Model

The MIMSLs as transceivers can be described by modifying the traveling wave model after taking into account external optical feedback and optical injection. To numerically demonstrate the proposed system, the simulation method is the split-step time domain model (SS-TDM), where the time-dependent coupled wave equations describing the active/passive waveguide devices are derived from Maxwell's equations as follows [31–33]:

$$\frac{1}{v_g}\frac{\partial E^+_{\mathrm{M,S}}(z,t)}{\partial t}+\frac{\partial E^+_{\mathrm{M,S}}(z,t)}{\partial z}=\left(G_{\mathrm{M,S}}-i\delta_{\mathrm{M,S}}-\frac{\alpha_0}{2}\right)E^+_{\mathrm{M,S}}(z,t)+ikE^-_{\mathrm{M,S}}(z,t)+\xi^+_{\mathrm{M,S}}(z,t), \quad (1)$$

$$\frac{1}{v_g}\frac{\partial E^-_{\mathrm{M,S}}(z,t)}{\partial t}-\frac{\partial E^-_{\mathrm{M,S}}(z,t)}{\partial z}=\left(G_{\mathrm{M,S}}-i\delta_{\mathrm{M,S}}-\frac{\alpha_0}{2}\right)E^-_{\mathrm{M,S}}(z,t)+ikE^+_{\mathrm{M,S}}(z,t)+\xi^-_{\mathrm{M,S}}(z,t), \quad (2)$$

where the subscripts M and S represent the MSL and the SSL, respectively. $E^+_{\mathrm{M,S}}$ (z, t) and $E^-_{\mathrm{M,S}}$ (z, t) are the forward and backward slowly varying amplitudes of the traveling optical fields in Equation (1) and Equation (2). $G_{\mathrm{M,S}}$ and $\delta_{\mathrm{M,S}}$ denote the field gain and detuning factor, respectively. $k = k_i + jk_g$ is the coupling coefficient, where k_i is the index-coupling coefficient, and k_g is the gain-coupling coefficient. $\xi^+_{\mathrm{M,S}}$ (z, t) and $\xi^-_{\mathrm{M,S}}$ (z, t) represent spontaneous emission noise generated by a Gaussian distributed random process.

The field gain is given by

$$G_{\mathrm{M,S}}=\frac{\Gamma g_N(N_{\mathrm{M,S}}-N_0)}{2(1+\varepsilon S_{\mathrm{M,S}})}, \quad (3)$$

where g_N is the differential gain, N_0 is the transparency carrier density, ε is the gain suppression coefficient and $S_{\mathrm{M,S}}$ is the photon density given by $|E^+_{\mathrm{M,S}}(z, t)|^2 + |E^-_{\mathrm{M,S}}(z, t)|^2$.

The detuning factor that describes the deviation from the Bragg condition is given by

$$\delta_{\mathrm{M,S}} = \frac{w_0}{c}\left(n_{eff} - \frac{\lambda_0}{4\pi}\Gamma\alpha_H g_N(N_{\mathrm{M,S}} - N_0)\right) - \frac{\pi}{\Lambda}, \tag{4}$$

where n_{eff} is the effective index of the waveguide at the Bragg wavelength, Λ is the period of the Bragg grating and α_H is the linewidth enhancement factor.

In the phase section, the injected carriers do not couple to the lasing fields, but cause a refractive index change. The detuning factor in the phase section is given by $\delta_{\mathrm{P}} = -(\varphi_{\mathrm{P}} + \pi V_{\mathrm{key}}/\mathrm{V}_{\pi})/(2L_{\mathrm{P}})$, where φ_{P} is the phase shift controlled by current injected and L_{P} is the length of the phase section. The phase shift is treated as a private key by phase modulation (PM). The PM driving signal is described as $V_{\mathrm{key}}(t) = A_0 \cos(2\pi f_0 t)$, where A_0 and f_0 stand for the amplitude and the frequency of the secret key signal, respectively.

The photon and carrier densities along the cavity are coupled through the carrier density equation as follows:

$$\frac{dN_{\mathrm{M,S}}}{dt} = \frac{I_{\mathrm{M,S}}}{qV} - AN_{\mathrm{M,S}} - BN_{\mathrm{M,S}}^2 - CN_{\mathrm{M,S}}^3 - v_g G_{\mathrm{M,S}} S_{\mathrm{M,S}}, \tag{5}$$

where $N_{\mathrm{M,S}}$ is the carrier density, $I_{\mathrm{M,S}}$ is the bias current, q is the electron charge, V is the active cavity volume, and A, B and C are the linear, bimolecular and Auger recombination coefficients, respectively.

According to the security system for unidirectional communication, the boundary condition for the forward and backward propagating waves at the facets can be written as:

$$E_{\mathrm{M,S}}^{+}(z = 0,\ t) = r_L E_{\mathrm{M,S}}^{-}(z = 0,\ t) + k_{inj} E_{\mathrm{M}}^{+}(z = 0, t - \tau), \tag{6}$$

$$E_{\mathrm{M,S}}^{-}(z = L, t) = r_R E_{\mathrm{M,S}}^{+}(z = L, t), \tag{7}$$

where r_L and r_R are the facet reflection coefficient at $z = 0$ and $z = L$, respectively. k_{inj} and τ are the injection coefficient and delay time of the MSL unidirectional to the SSL. The parameters used in the simulation are set by referring to Ref. [29], except for the lengths of the different sections, index grating coupling coefficient, etc. All the parameters are listed in Table 1.

Table 1. Simulation parameters of the MIMSL.

Parameter	Value
Central wavelength (λ_0)	1550 nm
Length of the DFB section (L_{DFB})	200 µm
Length of the Phase 1 section (L_{P1})	150 µm
Length of the SOA section (L_{SOA})	300 µm
Length of the Phase 2 section (L_{P2})	250 µm
Length of the waveguide (L_{W})	4 mm
Active region thickness (d)	0.15 µm
Active region width (w)	3 µm
Group refractive index (n_g)	3.7
Effective refractive index (n_{eff})	3.2
Index grating coupling coefficient (k_i)	110 cm $^{-1}$
Gain grating coupling coefficient (k_g)	11 cm $^{-1}$
Linewidth enhancement factor (α_H)	4
Transparency carrier density (N_0)	1.5×10^{18} cm $^{-3}$
Confinement factor (Γ)	0.3
Internal loss (α_0)	25 cm^{-1}
Linear recombination coefficient (A)	3×10^8 s^{-1}
Bimolecular recombination coefficient (B)	1×10^{-10} cm^3 s^{-1}
Auger recombination coefficient (C)	1.3×10^{-29} cm^6 s^{-1}
Nonlinear gain saturation coefficient (ε)	1×10^{-17} cm^3
Differential gain (g_N)	3×10^{-16} cm^2
Waveguide loss (α_{W})	5 cm^{-1}
Spontaneous coupling factor (β)	1×10^{-5}

A reasonable definition of the feedback strength (k_f) is

$$k_f = r_R \exp[-\alpha_0 L_{P1} - \alpha_0 L_{P2} + (G_{SOA} - \alpha_0)L_{SOA} - \alpha_W L_W], \quad (8)$$

where G_{SOA} is taken at the gain of the SOA section. The upper limit for k_f is set by the onset of gain saturation [34].

3. Results

3.1. Dynamic States

The MIMSL can work in various dynamic states, depending on the bias currents in the different sections. We set the bias current of the DFB section (I_{DFB}) to $2I_{th}$, where I_{th} = 14 mA was the laser threshold current, and the phase shifts of phase sections (φ_{P1} and φ_{P2}) were fixed to 0 and $\pi/2$. The dynamic states were controlled by the bias current of SOA section (I_{SOA}). Figure 2 shows the temporal waveforms, optical spectra, radio frequency (RF) spectra and phase portrait of the outputs signal.

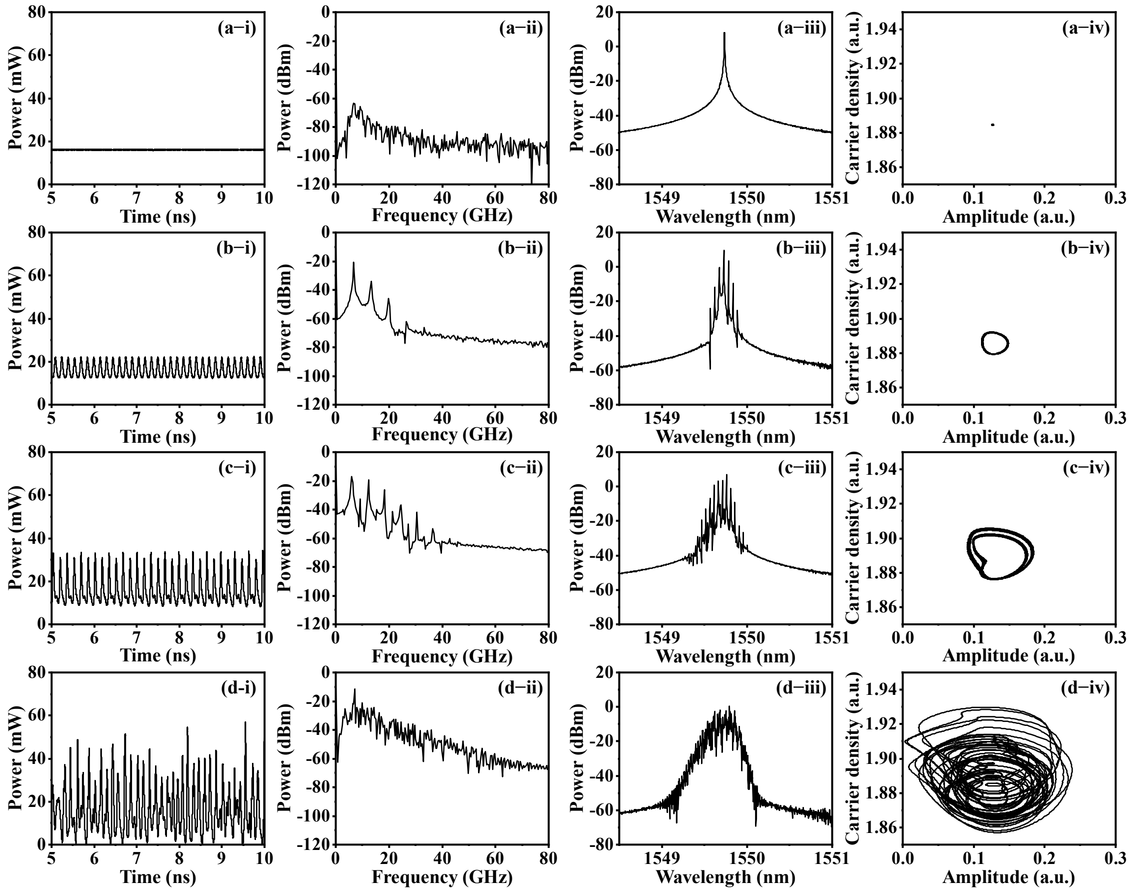

Figure 2. Various dynamic states of the MIMSL, I_{DFB} = $2I_{th}$, φ_{P1} = 0, φ_{P2} = $\pi/2$, when I_{SOA} varies from top to bottoms as (**a**) 14 mA (S state); (**b**) 15 mA (P-1 state); (**c**) 17 mA (P-2 state); (**d**) 24 mA (C state). (**a-i**)–(**d-i**) temporal waveforms, (**a-ii**)–(**d-ii**) RF spectra, (**a-iii**)–(**d-iii**) optical spectra, and (**a-iv**)–(**d-iv**) phase portraits of various dynamic states, respectively.

When I_{SOA} = 14 mA, Figure 2a-i–a-iv shows the laser working in the steady (S) state. The temporal waveform was almost a constant with small ripples due to the spontaneous radiation noise. The RF spectrum was similar to the noise floor except for a little bulge, which revealed the relaxation–oscillation frequency of about 6.7 GHz. The optical spectrum showed a typical single mode shape with a deviation of 0.27 nm, and the wavelength deviation was caused by the index grating coupling coefficient. When I_{SOA} increased to 15 mA, as shown in Figure 2b, the laser entered into the period-one (P-1) state, the optical spectra are displayed as a single mode state and the temporal waveform showed a single period oscillation trace. The P-1 state was also confirmed from the RF spectrum and the phase diagram, where a fundamental frequency appeared at around 6.7 GHz and trajectories of the phase portrait showed a clear limit cycle feature. When I_{SOA} increased to 17 mA, as shown in Figure 2c, the laser entered the period-two (P-2) state, multiple side modes appeared in the optical spectra and the temporal waveform showed a double period oscillation trace. The trajectories of the phase diagram showed a clear limit double cycle feature. Further increasing I_{SOA} to 24 mA, the device was driven into the chaos (C) state, which can be confirmed from Figure 2d. The optical spectrum was considerably broadened and the corresponding power spectrum covered a broad frequency range. Furthermore, the temporal waveform fluctuated dramatically, and the phase diagram showed a widely scattered distribution in a large area.

3.2. Chaos Synchronization

To numerically investigate the chaos synchronization performance of the unidirectional communication in Figure 1b, we set the control parameters of MIMSL as follows: $I_{\mathrm{DFB}} = 2I_{\mathrm{th}}$, $\varphi_{\mathrm{P1}} = 0$, $I_{\mathrm{SOA}} = 24$ mA, $\varphi_{\mathrm{P2}} = \pi/2$, which allowed the laser to operate in a chaotic state. The phase sections were modulated independently by the driving signals key 1 and key 2. For the key 1 and key 2, the modulation parameters were $A_1 = 0.5\ \mathrm{V}_\pi$, $f_1 = 10$ GHz and $A_2 = \mathrm{V}_\pi$, $f_2 = 10$ GHz, respectively. The SSL is not only equipped with identical feedback terms, but also suffers from unidirectional injection of the MSL. Here, we set the injection parameters as $k_{inj} = 0.36$ and $\tau = 0$ ns, while the information transmission rate was 2.5 Gb/s and the modulation depth of 0.05. For simplicity, we neglected the propagation-delay time.

The cross-correlation CC is used to evaluate the synchronization performance of parameter mismatch, which is defined by

$$CC = \frac{\langle [P_{\mathrm{M}}(t) - \langle P_{\mathrm{M}}(t)\rangle][P_{\mathrm{S}}(t) - \langle P_{\mathrm{S}}(t)\rangle]\rangle}{\sqrt{\langle [P_{\mathrm{M}}(t) - \langle P_{\mathrm{M}}(t)\rangle]^2\rangle\langle [\mathrm{P}_{\mathrm{S}}(t) - \langle P_{\mathrm{S}}(t)\rangle]^2\rangle}}, \tag{9}$$

where P_{M} and P_{S} are the output intensity waveforms of transmitter MSL and receiver SSL, respectively. $<\cdot>$ denote the time average.

Figure 3 shows the synchronization state of the transceivers for $k_{inj} = 0.36$ and $\tau = 0$ ns. The cross-correlation value of MSL and SSL was 0.965. Figure 3a,c show the temporal waveforms and the correlation plot. In Figure 3b, the RF spectra of the two lasers were similar at low frequency. This was due to the injection locking.

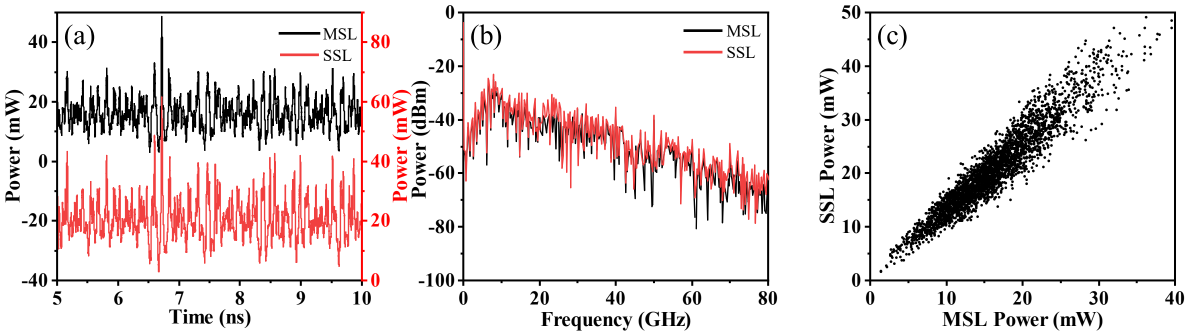

Figure 3. Synchronization diagram for two unidirectionally coupled modules in master/slave configuration. (**a**) Temporal waveforms, (**b**) RF spectra, (**c**) correlation plot.

Figure 4 shows the message encryption/decryption process for a message modulation depth of 0.05 and a transmission rate of 2.5 Gb/s. In Figure 4b, the message is completely hidden in the chaotic carrier wave. In Figure 4c, the temporal waveform of the input original message corresponds to the output decrypted message.

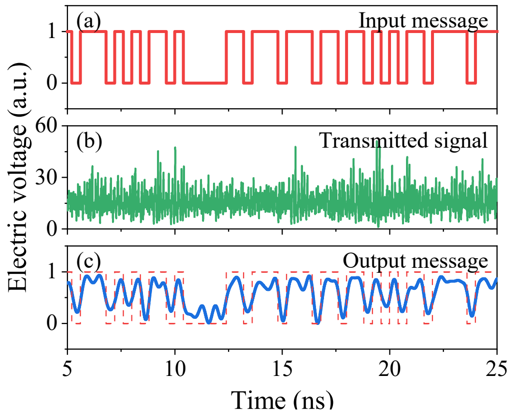

Figure 4. Illustration of message encryption/decryption processes. (**a**) The input original message, (**b**) the transmitted signal, and (**c**) the input original message (dashed) and output recovery message (solid).

3.3. Physical Key Space Analysis

The mismatch sensitivity of the tunable parameters of MIMSL is an important factor in determining the security of the system. One kind of parameter is represented by I_{DFB}, φ_{P1}, I_{SOA}, φ_{P2}. The other is the PM driving-signal parameter of each phase section, represented by the amplitude A and the frequency f of the signal. Based on the key space analysis method in [20], the physical key space is determined by the tuning ranges and the mismatch resolutions of the tunable parameters as follows: I_{DFB}, φ_{P1}, I_{SOA}, φ_{P2}, A_1, f_1, A_2 and f_2. According to reference [19], we set the synchronization threshold of *CC* coefficient to 0.9.

Figure 5 displays the synchronization coefficient as a function of the bias current mismatch in the DFB and SOA sections. In Figure 5a, the critical mismatch of I_{DFB} is 4.4 mA. It can be seen that the SSL achieved good synchronization performance, when the bias current mismatch value was less than 0. This is because the SSL is in a locked injection state by increasing the injection strength. As the bias current mismatch value increased, the SSL was no longer injection locked, resulting in a decrease in the synchronization coefficient. According to the threshold current of 14 mA for the DFB section and a maximum bias current of 100 mA, the tunable range of the bias current was 86 mA. The key number of I_{DFB} was N_{DFB} = 86/4.4 = 19. In Figure 5b, the critical mismatch of I_{SOA} was 1.6 mA. As the I_{SOA} was below the threshold gain current, the SOA section induced absorbing to attenuate the feedback light. When I_{SOA} is greater than the threshold gain value, the section has an amplifying effect on the feedback light. Here, I_{SOA} was set to the maximum of 100 mA, and the tunable range of I_{SOA} was 100 mA. The key number of I_{SOA} was N_{SOA} = 100/1.6 = 62.

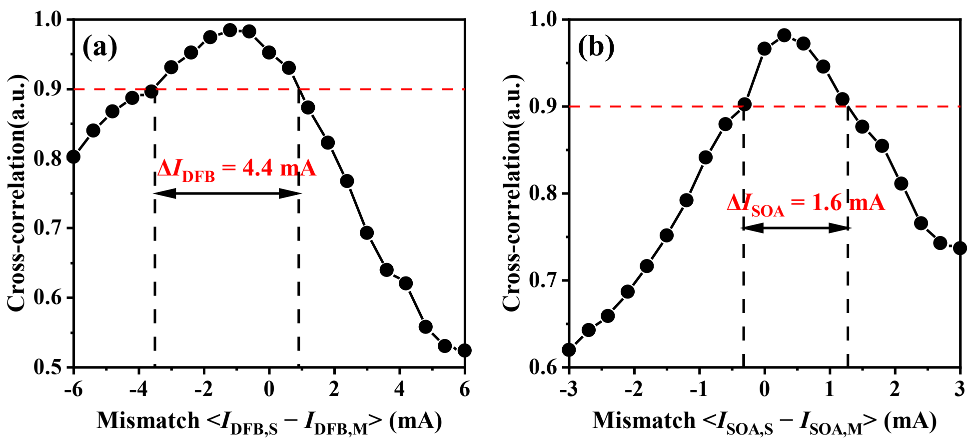

Figure 5. Influence of the bias current of (**a**) DFB laser section ($I_{DFB} = 2I_{th}$) and (**b**) SOA section (I_{SOA} = 24 mA) mismatch on chaotic synchronization coefficients.

Figure 6 illustrates the synchronization coefficient as a function of the phase shift of each phase section mismatch. Indicated by the synchronization threshold, the critical mismatches for the phase shifts of φ_{P1} and φ_{P2} were 0.22π and 0.20π. As the period of the phase change was 2π, the key number of the phase shift of the Phase 1 section was $N_{P1} = 2\pi/0.22\pi = 9$, and for the Phase 2 section was $N_{P2} = 2\pi/0.20\pi = 10$.

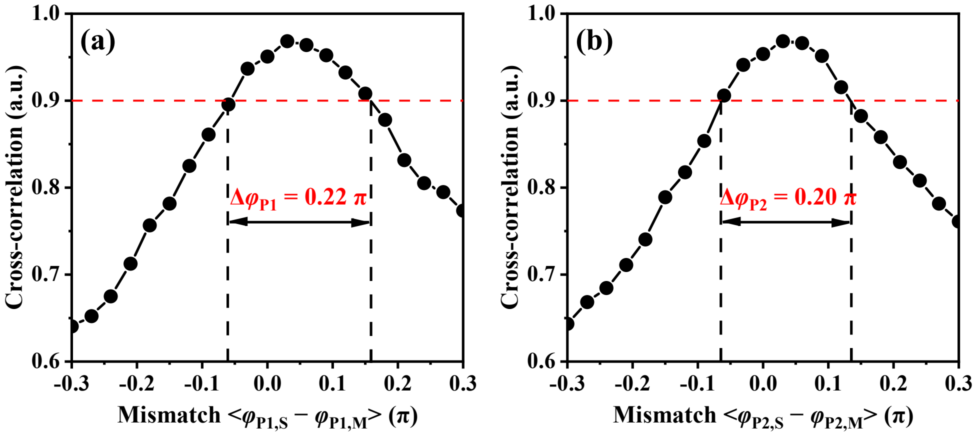

Figure 6. Influence of the phase shift of phase sections mismatch on chaotic synchronization coefficients: (**a**) the phase shift of Phase 1 section ($\varphi_{P1} = 0$) and (**b**) the phase shift of Phase 2 section ($\varphi_{P2} = \pi/2$).

Figures 7 and 8 depict the synchronization coefficient as a function of the parameter mismatches in the phase sections for the amplitude A and the frequency f of the PM driving signal. Considering the availability of the common commercial devices, the maximum tuning range of A was set as 4 V_π, and 40 GHz for f. As shown in Figure 7, the critical mismatches of A_1 and A_2 were 0.29 V_π and 0.25 V_π, respectively. As shown in Figure 8, the critical mismatches of f_1 and f_2 were as small as about 14 MHz and 7 MHz, respectively. The difference in the PM driving signal mismatch between the Phase 1 and Phase 2 sections was caused by the amplitude of the PM driving signal. The key number of the PM driving signal in phase sections was $N_{key} = N_{A1}\, N_{A2}\, N_{f1}\, N_{f2} = 3.395{,}578{,}784 \times 10^9$.

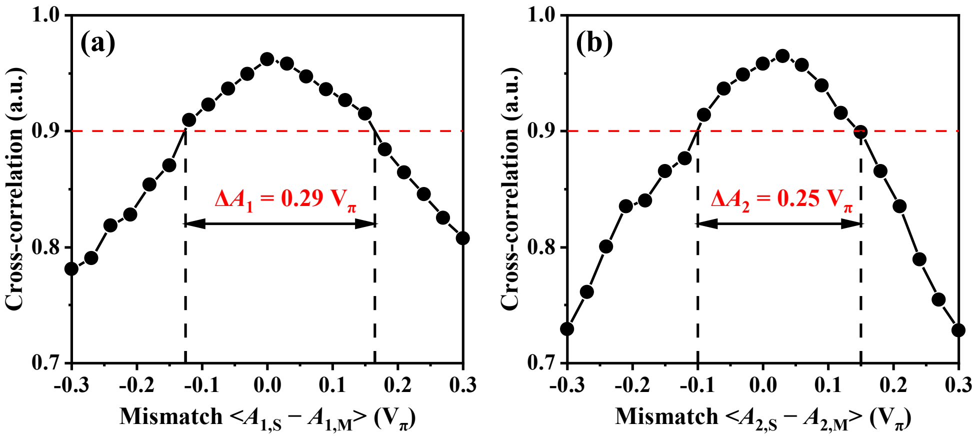

Figure 7. Influence of PM driving signal in the phase sections mismatch on chaotic synchronization coefficients: (**a**) the amplitude index ($A_1 = 0.5\ V_\pi$) in the Phase 1 section and (**b**) the amplitude index ($A_2 = V_\pi$) in the Phase 2 section.

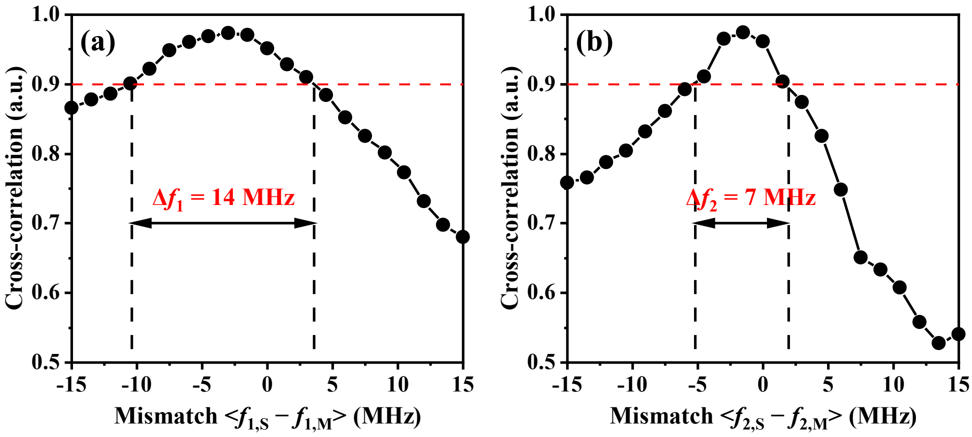

Figure 8. Influence of PM driving signal in the phase sections mismatch on chaotic synchronization coefficients: (**a**) the frequency (f_1 = 10 GHz) in the Phase 1 section and (**b**) the frequency (f_2 = 10 GHz) in the Phase 2 section.

As a result, the total key space of the MIMSL is calculated as $N = N_{DFB}\ N_{P1}\ N_{SOA}\ N_{P2}\ N_{key} = 3.6 \times 10^{14}$ (about 2^{48}) at a data rate of 2.5 Gb/s and an injection strength of 0.36.

4. Discussion

Compared with chaotic secure communication systems composed of discrete devices, integrated photonic chips are small in size, low in cost, highly functional and highly integrated. In this work, we propose the MIMSL as a chaotic transceiver to provide a new idea for enhancing the key space of chaotic secure communication systems. Through theoretical and numerical studies, we demonstrate that our proposed MIMSL integrates a huge additional key space. Furthermore, by optimizing the structural parameters and size of the photonic chip, we have taken another step towards a highly integrated on-chip chaotic transceiver and transmitter for chaotic secure communication systems. Having solved the security problem of chaotic optical secure communication, we believe that the application of photonic chips to key distribution, chaotic lidar, and random number generation will become more important topics, and related work is currently under investigation. We expect that this research will provide more guidance for chaotic optical communication in practical applications.

5. Conclusions

In conclusion, we have proposed and numerically demonstrated the security enhancement of a MIMSL-based chaotic communication, which depends not only on the difficulty of identifying the MIMSL parameters, but also on the phase shifts as keys to encrypt the phase of the feedback light in the MIMSL. The numerical study shows that the chaotic synchronization of MIMSL is more sensitive to parameter mismatch. Therefore, with 2.5 Gb/s data transmission, the dimension of the key space is enlarged, the total size of key space achieved is 2^{48}, and the security of data transmission is greatly improved.

Author Contributions: Conceptualization, Y.W. and Y.S.; methodology, F.Z.; software, F.Z. and J.X.; writing—original draft preparation, F.Z. and Y.S.; writing—review and editing, Y.W., Y.S. and P.L.; supervision, A.W. and Y.Q.; All authors have read and agreed to the published version of the manuscript.

Funding: This research was funded by the National Key Research and Development Program of China (grant no. 2019YFB1803500), the National Natural Science Foundation of China (grant nos. 61731014, U22A2087, and 61961136002).

Institutional Review Board Statement: Not applicable.

Informed Consent Statement: Not applicable.

Data Availability Statement: The data presented in this study are available on request from the corresponding author.

Conflicts of Interest: The authors declare no conflict of interest.

References

1. Pecora, L.M.; Carroll, T.L. Synchronization in chaotic systems. *Phys. Rev. Lett.* **1990**, *64*, 821. [CrossRef]
2. Vanwiggeren, G.D.; Roy, R. Communication with chaotic lasers. *Science* **1998**, *279*, 1198–1200. [CrossRef]
3. Argyris, A.; Syvridis, D.; Larger, L.; Annovazzi-Lodi, V.; Colet, P.; Fischer, I.; García-Ojalvo, J.; Mirasso, C.R.; Pesquera, L.; Shore, K.A. Chaos-based communications at high bit rates using commercial fibre-optic links. *Nature* **2005**, *438*, 343–346. [CrossRef] [PubMed]
4. Huang, C.; Gao, X.; Wu, S.; Gu, W.; Su, B.; Wang, Y.; Qin, Y.; Gao, Z. Key Space Enhanced Correlated Random Bit Generation Based on Synchronized Electro-Optic Self-Feedback Loops with Mach–Zehnder Modulators. *Photonics* **2022**, *9*, 952. [CrossRef]
5. Mbé, J.H.T.; Atchoffo, W.N.; Tchitnga, R.; Woafo, P. Dynamics of time-delayed optoelectronic oscillators with nonlinear amplifiers and its potential application to random numbers generation. *IEEE J. Quantum Electron.* **2021**, *57*, 1–7.
6. Cui, B.; Xia, G.; Tang, X.; Wang, Y.; Wu, Z. Fast physical random bit generation based on a chaotic optical injection system with multi-path optical feedback. *Appl. Opt.* **2022**, *61*, 8354–8360. [CrossRef] [PubMed]
7. Gao, Z.; Wu, S.; Deng, Z.; Huang, C.; Gao, X.; Fu, S.; Li, Z.; Wang, Y.; Qin, Y. Private correlated random bit generation based on synchronized wideband physical entropy sources with hybrid electro-optic nonlinear transformation. *Opt. Lett.* **2022**, *47*, 3788–3791. [CrossRef]
8. Lin, F.Y.; Liu, J.M. Chaotic lidar. *IEEE J. Sel. Top. Quantum Electron.* **2004**, *10*, 991–997. [CrossRef]
9. Wang, Y.; Zhang, M.; Zhang, J.; Qiao, L.; Wang, T.; Zhang, Q.; Zhao, L.; Wang, Y. Millimeter-level-spatial-resolution Brillouin optical correlation-domain analysis based on broadband chaotic laser. *J. Lightwave Technol.* **2019**, *37*, 3706–3712. [CrossRef]
10. Zhao, T.; Han, H.; Zhang, J.; Liu, X.; Chang, X.; Wang, A.; Wang, Y. Precise fault location in TDM-PON by utilizing chaotic laser subject to optical feedback. *IEEE Photonics J.* **2015**, *7*, 1–9. [CrossRef]
11. Zhang, M.; Liu, T.; Wang, A.; Zheng, J.; Meng, L.; Zhang, Z.; Wang, Y. Photonic ultrawideband signal generator using an optically injected chaotic semiconductor laser. *Opt. Lett.* **2011**, *36*, 1008–1010. [CrossRef] [PubMed]
12. Bogris, A.; Rizomiliotis, P.; Chlouverakis, K.E.; Argyris, A.; Syvridis, D. Feedback phase in optically generated chaos: A secret key for cryptographic applications. *IEEE J. Quantum Electron.* **2008**, *44*, 119–124. [CrossRef]
13. Xue, C.; Jiang, N.; Lv, Y.; Wang, C.; Li, G.; Lin, S.; Qin, K. Security-enhanced chaos communication with time-delay signature suppression and phase encryption. *Opt. Lett.* **2016**, *41*, 3690–3693. [CrossRef] [PubMed]
14. Deng, T.; Xia, G.; Wu, Z.; Lin, X.; Wu, J. Chaos synchronization in mutually coupled semiconductor lasers with asymmetrical bias currents. *Opt. Express* **2011**, *19*, 8762–8773. [CrossRef]
15. Sasaki, T.; Kakesu, I.; Mitsui, Y.; Rontani, D.; Uchida, A.; Sunada, S.; Yoshimura, K.; Inubushi, M. Common-signal-induced synchronization in photonic integrated circuits and its application to secure key distribution. *Opt. Express* **2017**, *25*, 26029–26044. [CrossRef]
16. Nguimdo, R.M.; Verschaffelt, G.; Danckaert, J.; Sande, G.V. Loss of time-delay signature in chaotic semiconductor ring lasers. *Opt. Lett.* **2012**, *37*, 2541–2543. [CrossRef]
17. Xiang, S.; Pan, W.; Zhang, L.; Wen, A.; Shang, L.; Zhang, H.; Lin, L. Phase-modulated dual-path feedback for time delay signature suppression from intensity and phase chaos in semiconductor laser. *Opt. Commun.* **2014**, *324*, 38–46. [CrossRef]
18. Li, S.; Liu, Q.; Chan, S. Distributed feedbacks for time-delay signature suppression of chaos generated from a semiconductor laser. *IEEE Photonics J.* **2012**, *4*, 1930–1935.
19. Wang, D.; Wang, L.; Zhao, T.; Gao, H.; Wang, Y.; Chen, X.; Wang, A. Time delay signature elimination of chaos in a semiconductor laser by dispersive feedback from a chirped FBG. *Opt. Express* **2017**, *25*, 10911–10924. [CrossRef]
20. Hou, T.; Yi, L.; Yang, X.; Ke, J.; Hu, Y.; Yang, Q.; Zhou, P.; Hu, W. Maximizing the security of chaotic optical communications. *Opt. Express* **2016**, *24*, 23439–23449. [CrossRef]
21. Wang, C.; Ji, Y.; Wang, H.; Bai, L. Security-enhanced electro-optic feedback phase chaotic system based on nonlinear coupling of two delayed interfering branches. *IEEE Photonics J.* **2018**, *10*, 1–15. [CrossRef]
22. Argyris, A.; Hamacher, M.; Chlouverakis, K.E.; Bogris, A.; Syvridis, D. Photonic integrated device for chaos applications in communications. *Phys. Rev. Lett.* **2008**, *100*, 194101. [CrossRef] [PubMed]
23. Argyris, A.; Grivas, E.; Hamacher, M.; Bogris, A.; Syvridis, D. Chaos-on-a-chip secures data transmission in optical fiber links. *Opt. Express* **2010**, *18*, 5188–5198. [CrossRef] [PubMed]
24. Tronciu, V.Z.; Mirasso, C.R.; Colet, P.; Hamacher, M.; Benedetti, M.; Vercesi, V.; Annovazzi-Lodi, V. Chaos generation and synchronization using an integrated source with an air gap. *IEEE J. Quantum Electron.* **2010**, *46*, 1840–1846. [CrossRef]
25. Harayama, T.; Sunada, S.; Yoshimura, K.; Davis, P.; Tsuzuki, K.; Uchida, A. Fast nondeterministic random-bit generation using on-chip chaos lasers. *Phys. Rev. A* **2011**, *83*, 031803. [CrossRef]
26. Takahashi, R.; Akizawa, Y.; Uchida, A.; Harayama, T.; Tsuzuki, K.; Sunada, S.; Arai, K.; Yoshimura, K.; Davis, P. Fast physical random bit generation with photonic integrated circuits with different external cavity lengths for chaos generation. *Opt. Express* **2014**, *22*, 11727–11740. [CrossRef]

27. Ugajin, K.; Terashima, Y.; Iwakawa, K.; Uchida, A.; Harayama, T.; Yoshimura, K.; Inubushi, M. Real-time fast physical random number generator with a photonic integrated circuit. *Opt. Express* **2017**, *25*, 6511–6523. [CrossRef]
28. Wu, J.; Zhao, L.; Wu, Z.; Lu, D.; Tang, X.; Zhong, Z.; Xia, G. Direct generation of broadband chaos by a monolithic integrated semiconductor laser chip. *Opt. Express* **2013**, *21*, 23358–23364. [CrossRef]
29. Yu, L.; Lu, D.; Pan, B.; Zhao, L.; Wu, J.; Xia, G.; Wu, Z.; Wang, W. Monolithically integrated amplified feedback lasers for high-quality microwave and broadband chaos generation. *J. Lightwave Technol.* **2014**, *32*, 3595–3601. [CrossRef]
30. Qi, H.; Chen, G.; Lu, D.; Zhao, L. A monolithically integrated laser-photodetector chip for on-chip photonic and microwave signal generation. *Photonics* **2019**, *6*, 102. [CrossRef]
31. Kim, B.S.; Chung, Y.; Lee, J.S. An efficient split-step time-domain dynamic modeling of DFB/DBR laser diodes. *IEEE J. Quantum Electron.* **2000**, *36*, 787–794.
32. Bauer, S.; Brox, O.; Kreissl, J.; Sartorius, B.; Radziunas, M.; Sieber, J.; Wünsche, H.J.; Henneberger, F. Nonlinear dynamics of semiconductor lasers with active optical feedback. *Phys. Rev. E* **2004**, *69*, 016206. [CrossRef] [PubMed]
33. Zhao, G.; Sun, J.; Xi, Y.; Gao, D.; Lu, Q.; Guo, W. Design and simulation of two-section DFB lasers with short active-section lengths. *Opt. Express* **2016**, *24*, 10590–10598. [CrossRef]
34. Brox, O.; Bauer, S.; Radziunas, M.; Wolfrum, M.; Sieber, J.; Kreissl, J.; Sartorius, B.; Wunsche, H.J. High-frequency pulsations in DFB lasers with amplified feedback. *IEEE J. Quantum Electron.* **2003**, *39*, 1381–1387. [CrossRef]

Disclaimer/Publisher's Note: The statements, opinions and data contained in all publications are solely those of the individual author(s) and contributor(s) and not of MDPI and/or the editor(s). MDPI and/or the editor(s) disclaim responsibility for any injury to people or property resulting from any ideas, methods, instructions or products referred to in the content.